Microstructure-informed statistical modelling of cleavage fracture in high strength steels considering through-thickness inhomogeneities

Jiang, Quanxin; Bertolo, V. M.; Popovich, V. A.; Sietsma, J.; Walters, Carey L.

Important note
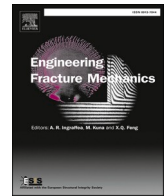To cite this publication, please use the final published version (if applicable).
Please check the document version above.

Microstructure-informed statistical modelling of cleavage fracture in high strength steels considering through-thickness inhomogeneities

Quanxin Jiang [a,*], V.M. Bertolo [a], V.A. Popovich [a], J. Sietsma [a], Carey L. Walters [b,c]

[a] *Department of Materials Science and Engineering, Delft University of Technology, Delft, the Netherlands*
[b] *Department of Maritime and Transport Technology, Delft University of Technology, Delft, the Netherlands*
[c] *Structural Dynamics, TNO, Delft, the Netherlands*

ABSTRACT

Thick section S690 QT steel is modelled with a modified multibarrier model that is based on the weakest-link mechanism. Segregation bands are modelled as discrete layers which have different grain size, yield properties, and local fracture parameters from outside of the bands. The results show that embrittlement from segregation bands can only be adequately reflected if the in-homogeneities of the fracture parameters are accounted for. The present methodology quantitively captures the cooperation of complex microstructural features in cleavage and can facilitate the trade-off between the effects of various microstructural parameters in toughness control.

1. Introduction

Toughness of ferritic steels at low temperatures and the ductile-to-brittle transition temperature region are related to transgranular quasi-cleavage fracture, which will be called cleavage in this paper. In most engineering applications, the trade-off between various controllable parameters (e.g. weld travel speed, process, wire composition, cooling rate, etc.) to generate both cost-effective and sufficiently tough base metal/weld/HAZ (heat-affected zone) combination is accepted (e.g. [1]). These processing parameters determine the microstructure of the material, such as prior austenite grain size [2], carbide size [3], the presence of inclusions [4], M-A (martensite-austenite) phases [5], precipitates, etc. (for an overview, see [6]). As a highly localized phenomenon, cleavage fracture exhibits strong sensitivity to material characteristics at the microstructural level, dependent on composition and structure fabrication, and it is coupled with a constraint effect originating from the macroscopic stress state. This coupling complicates the development of fracture mechanics assessments based on available standard specimen data. Many studies have attempted to correlate the toughness and microstructural parameters of steels [3–11], but most of them are descriptive rather than predictive.

The local approach to cleavage fracture is a class of physically-driven statistical models that account for the probability of failure based on the local stress (and sometimes strain) field [12–14] proposed the Weibull formulation based on the weakest-link mechanism. Following these studies, many attempts were made to quantitatively predict the scatter in the toughness [15–20]. More recently, other studies have tried to predict the toughness of steels from their microstructural parameters [21–23]. These efforts have shown the potential effectiveness of the local approach to cleavage fracture. However, the gradient of properties through the thickness and welded zones makes it impossible to predict and control cleavage fracture based only on a single microstructural region [24–26].

The need for more accurate cleavage modelling is particularly acute for a new generation of high- and very high-strength steels (yield strength of 500 to 1300 MPa) because they obtain their favorable properties through complex, multi-phase microstructures, which complicates microstructural modelling of cleavage-driven failure. The rolling of thick plates can also give rise to so-called segregation bands or spatial segregation of both alloying and impurity elements [27,28]. The consequence of such inhomogeneous and multiphase microstructures is a large scatter of properties through the thickness.(e.g. [29]). It is reported that up to 90% of brittle failure originates from the middle third of the material thickness [30], which indicates the importance of the centerline and possible segregation zones [31]. Macroscopic inhomogeneities, including macrosegregation and HAZ, have been modelled by bimodal methods [32–33], where the variations in cleavage properties are represented by macroscopic toughness parameters. The bimodal methods are not applicable to modelling segregation bands that are too small to extract specimens to determine those macroscopic parameters. Hence, to judge the susceptibility of such steel structures to catastrophic failures and to design future generations of improved steels, a quantitative, physically-based method taking into account the statistical and multi-parametric nature of steel microstructures is required.

A statistical method is proposed in this paper for the modelling of cleavage fracture based on microstructural parameters. The statistical model is a multi-barrier model that accounts for microcrack nucleation at hard inclusions and microcrack propagation based on the weakest-link mechanism. This model is validated with previously published experimental data, which includes specimens of S690 QT steel plate fractured at $-100\,^{\circ}$C and corresponding characterization of microstructures. Specimens taken from top quarter and middle-section of the plate have different microstructures, and their measured crack tip opening displacement (CTOD) values differ significantly. Centerline segregation bands appear in the middle section specimens, producing significant inhomogeneities. Approaches of modelling the segregation bands ("Yield and grain size variation method" and "Cleavage variation method") are compared in this paper to determine the transferability of microstructural fracture parameters through the thickness and to investigate the total effect of segregation bands on cleavage fracture.

2. Model description

2.1. Micromechanism of cleavage fracture

The model developed in this paper is based on a multiple-barrier theory of the cleavage mechanism [34–37]. The modelling of fracture toughness is based on a local fracture criterion and then is upscaled from unit volume to a specimen.

In the proposed model, cleavage fracture of ferritic steels is regarded as the result of successive occurrence of three events (Fig. 1):

I: nucleation of the slip-induced crack at a brittle second-phase particle (i.e. carbides in steels) or inclusion. Plastic flow is a necessary precursor, which might be by slipping or twinning.

II: propagation of the microcrack across the particle/matrix interface under the local stress state.

III: propagation of the grain-sized crack to neighbouring grains across the grain boundary under the local stress state.

Inclusions and second phase particles are associated with the fracture initiation (event I). Under plastic flow, stress in a second phase particle is raised to a level to nucleate a microcrack. If the particle is brittle and deforms elastically during cracking, a single-parameter condition can be motivated for crack nucleation, where a critical-strain-based model can be transformed into a critical-stress-based model. The stress level needed for inclusion cleavage is characterized by critical particle strength σ_H^C. Based on observations in [13,18], hard particle cracking only occurs after local yielding of the matrix, and the number of cracked particles is found to be in proportion to plastic strain in notched tensile bar tests. These facts indicate that σ_H^C is commonly higher than the peak stress in a specimen at the start of local yielding, and σ_H^C shows noticeable scatter. Here it is assumed the value of inclusion strength is uniformly distributed in the range $[\sigma_H^C, \sigma_H^C + \Delta\sigma_H^C]$, as shown in Fig. 2. For a volume that contains N inclusions, the number of cracked inclusions (N_{cr}) is in proportion to the inclusion stress σ_H and can be calculated as

$$N_{cr} = \min\{N \times (\sigma_H - \sigma_H^C)/\Delta\sigma_H^C, N\} \qquad (2\text{-}1)$$

Where the inclusion stress σ_H is calculated from the first principal stress of the matrix $\sigma_{1,matrix}$ and the equivalent von-mises stress of the matrix $\sigma_{eq,matrix}$, by
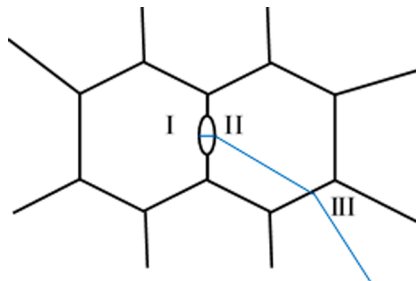

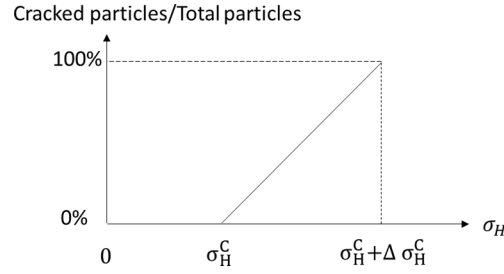**Fig. 1.** Critical events of cleavage fracture.

Fig. 2. Number of cracked particles vs maximum principal stress inside hard particles.

$$\sigma_H = \sigma_{1,matrix} + f_\alpha \sigma_{eq,matrix} \tag{2-2}$$

and the factor f_α is determined using the analytical solution in [38] based on the inclusion geometry. In eq. (2)-(2), $\sigma_{eq,matrix}$ increases with plastic strain for a strain-hardening material, and f_α is always positive for an elastic inclusion. As a result, the calculated inclusion stress σ_H increases with plastic strain, and given eq. (2)-(1), the number of cracked particles also increases with plastic strain.

Phase boundaries and grain boundaries in ferritic steels offer important resistance to the propagation of cleavage cracks (event II and III). The critical stress is usually used as a criterion for the crack propagation across the particle/matrix interface or across the grain boundary. The critical stress for a micro-crack to propagate within a grain has been related to the Griffith theory [39] based on energy balance. [6] has confirmed that an approximate relationship between σ_f (fracture stress) and $D^{-1/2}$ (root of grain diameter) exists. In the present paper, the particle/matrix interface strength is characterized by the local cleavage parameter K_{Ia}^{pm} and the grain boundary
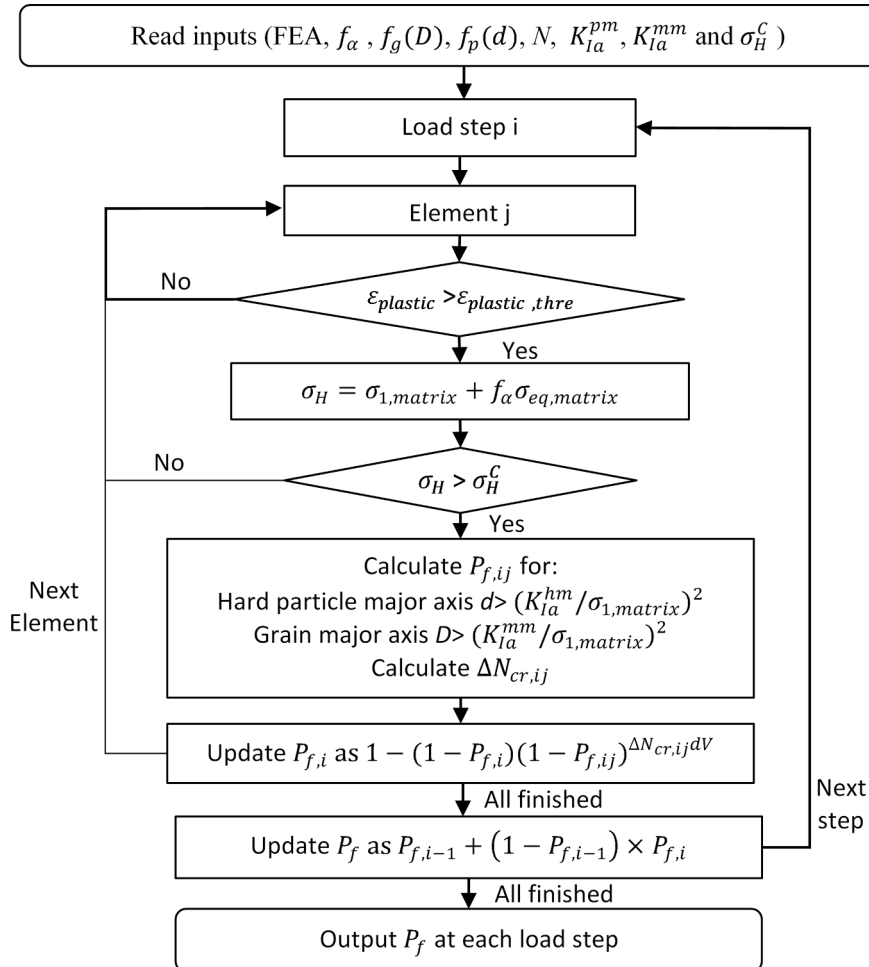

Fig. 3. Flow chart of the computational scheme.

strength is characterized by the local cleavage parameter K_{Ia}^{mm}. A minimum particle size (d_c) and a minimum grain size (D_c) are calculated for the first principal stress within the grain ($\sigma_{1,matrix}$) to propagate the micro-crack across the particle/matrix interface and grain boundary, by:

$$d_c = (K_{Ia}^{pm}/\sigma_{1,matrix})^2 \tag{2-3}$$

$$D_c = (K_{Ia}^{mm}/\sigma_{1,matrix})^2 \tag{2-4}$$

2.2. Microstructure-informed statistical model

This section outlines the computational model to calculate the cleavage probability of macroscale specimens. Finite element analysis (FEA) of a macroscopic volume gives the result of stress/strain distribution under a certain global load level. The stress calculated from FEA of each finite element will be used to calculate the cleavage probability of that finite element. The cleavage probability is calculated from a cleavage check based on the stress level, shape of the stress field, and statistical information of the microstructure. For a certain microstructure, the failure probability is a function of stress level and will be evaluated based on the volume of finite element. By accounting for the cleavage probability of all finite elements in the fracture process zone (areas that are plastically deforming), the total failure probability of the specimen can be calculated and can be expressed as a function of the global load. Fig. 3 gives a flow chart of the computational model to calculate the cleavage probability of macroscale specimens. The required inputs include FEA results (which contain $\sigma_{1,matrix}$, $\sigma_{eq,matrix}$, and $\varepsilon_{plastic}$ values within each finite element at each load increment), f_α calculated from inclusion geometry, the distribution density function of the grain major axis $f_g(D)$, the distribution density function of the hard particle major axis $f_p(d)$, number of inclusions N per elementary volume, cleavage parameters K_{Ia}^{pm}, K_{Ia}^{mm} and σ_H^C. Other parameters need to be defined are threshold plastic strain $\varepsilon_{plastic,thre}$, elementary volume V_0, and scatter of the inclusion fracture strength $\Delta\sigma_H^C$. Further explanation and definitions of the process depicted in Fig. 3 are given in the following paragraphs.

The cleavage probability of element j under load level i is noted as $P_{f,ij}$, and the cleavage probability of the specimen in the load increment i is noted as $P_{f,i}$. The cumulative cleavage probability of the specimen is calculated based on the following steps:

(1) Calculate the inclusion stress from $\sigma_H = \sigma_{1,matrix} + f_\alpha\sigma_{eq,matrix}$ and check if the inclusion stress exceeds the critical value σ_H^C.
(2) If the inclusion stress exceeds the critical value to nucleate a crack (σ_H^C), a minimum inclusion size d_c and a minimum grain size D_c are calculated for the first principal stress within the grain ($\sigma_{1,matrix}$) to propagate the crack across interface or boundary.
(3) A cleavage probability $P_{f,ij}$ is calculated as the integral of probability density that hard particles larger than the minimum particle size d_c and grains larger than the minimum grain size D_c, by

$$P_{f,ij} = \int_{D_c}^{+\infty} f_g(D)\mathrm{d}D \int_{d_c}^{+\infty} f_p(d)\mathrm{d}d \tag{2-5}$$

(4) If $\sigma_{H,i} > \sigma_{H,i-1}$, the number of newly cracked inclusions ΔN_{cr} per elementary volume (V_0) is calculated by

$$\Delta N_{cr} = N \times (min\{\sigma_{H,i}, \sigma_H^C + \Delta\sigma_H^C\} - max\{\sigma_{H,i-1}, \sigma_H^C\})/\Delta\sigma_H^C \tag{2-6}$$

(5) The cleavage probability $P_{f,ij}$ of the element j is modified based on the number of newly cracked inclusions and volume of the finite element V_j. The cleavage probability $P_{f,i}$ of the specimen in the load increment i is updated as $1 - (1 - P_{f,i})(1 - P_{f,ij})^{\Delta N_{cr}V_j/V_0}$.
(6) If the inclusion stress exceeds the critical value $\sigma_H^C + \Delta\sigma_H^C$, which means the number of cracked inclusions reaches N per elementary volume, the corresponding finite element will be deactivated for the rest of load steps for cleavage (which implies that the element still carries load but is assumed to not contain any newly cracked inclusions).
(7) After looping over all finite elements, the cumulative cleavage probability of the specimen is updated as:

$$P_f = P_{f,i-1} + (1 - P_{f,i-1}) \times P_{f,i} \tag{2-7}$$

When the computation is finished, the output is the fracture probability of each load step, in terms of CTOD value. This procedure is shown in Fig. 3.

Table 1
Chemical composition of S690 QT [40].

wt (%)	Fe	C	Si	Al	Mo	Other
Top	Bal.	0.17 ± 0.001	0.29 ± 0.022	0.07 ± 0.005	0.30 ± 0.007	Mn, Ni, Cr, Nb
Middle	Bal.	0.160 ± 0.001	0.30 ± 0.03	0.08 ± 0.01	0.29 ± 0.02	

3. Material

A commercially available 80 mm thick quenched and tempered S690 high strength steel plate is used in this paper for illustration and validation of the developed model. Materials are extracted from the top quarter section and the middle section of the plate. The materials have been previously characterized in [40,41]. The chemical composition of top quarter and middle sections of the steel plate was studied by XRF (X-ray fluorescence) and LECO combustion analysis [40]. The chemical composition of the steel plate is shown in Table 1.

The through thickness microstructure of the steel plate was analysed by means of scanning electron microscopy (SEM) with 5% Nital immersion etching for 15 s [40]. The microstructure of the plate varies through the thickness from a fully tempered martensitic structure in the regions close to the surfaces to a mixed tempered martensitic-bainitic structure in the middle section of the plate. Centreline segregation bands (CLs) appear in the middle section.

3.1. Volume fraction and spacing of CLs

It is observed that the CLs form layers parallel to the rolling direction and are sparsely distributed near the centreline of the plate, as shown in Fig. 4 (a). The section containing the CLs has an average thickness of approximately 8 mm. Microscopic image (Fig. 4 b) shows RD, ND plane intersecting the CLs. The mean thickness of each band is measured as 0.1 mm. The mean spacing between bands is measured as 0.2 mm.

3.2. Grain size

For the prior austenite grain (PAG) investigation, samples were swab etched with 100 ml saturated aqueous picric acid solution and 0.5 g of sodium dodecyl benzene sulfonate etching for 5 min [41]. From analysis on the reconstructed Prior Austenite Grains (PAG) the statistical distribution of grain size has been measured in the top section, within CLs and outside CLs in the middle section of the steel plate. Fig. 5 shows one example of the reconstructed PAG map in the middle section.

To quantify the grain size in cleavage modelling, least-square fitting is performed on the grain size data to get the function representing the distribution:

$$P(\text{majoraxis} > D) = \min\left\{1 - \text{lognormalCDF}(D, \mu, S), \frac{\alpha}{D^\beta}\right\} \tag{3-1}$$

where α and β are fitting parameters, and $\text{lognormalCDF}(D, \mu, S)$ represents equation $1/2 + 1/2 erf(\frac{lnD - \mu}{\sqrt{2}S})$, where μ is the mean and S is the standard deviation.

Fig. 6 shows the grain size data with the fit of eq. (3)-(1), with the fitting parameters in Table 2, zoomed in on the large grains. Note that because eq. (3)-(1) is a composite of two distributions that it might become discontinuous in the transition from one distribution to the other. The top sections have smaller grains and the microstructure outside CLs in the middle section has larger grains, while CLs have an intermediate grain size.
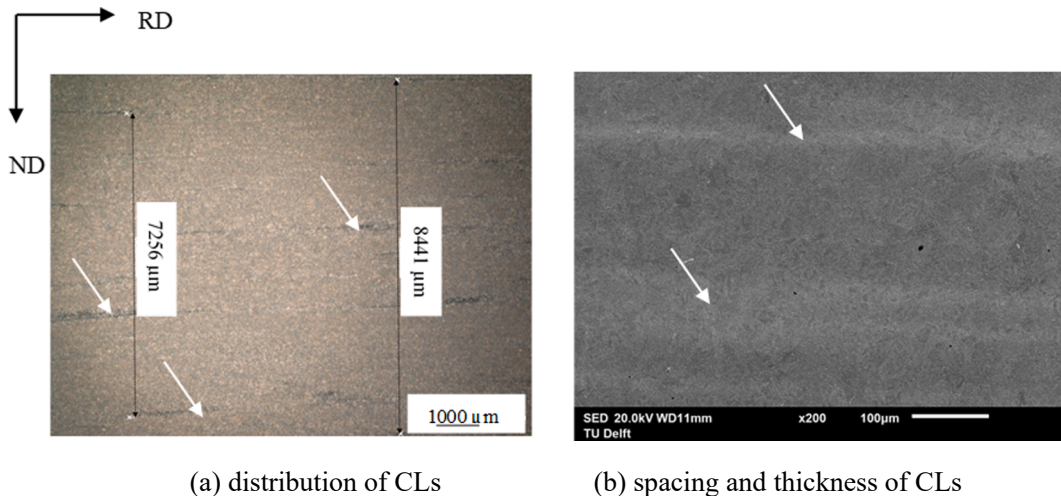

(a) distribution of CLs   (b) spacing and thickness of CLs

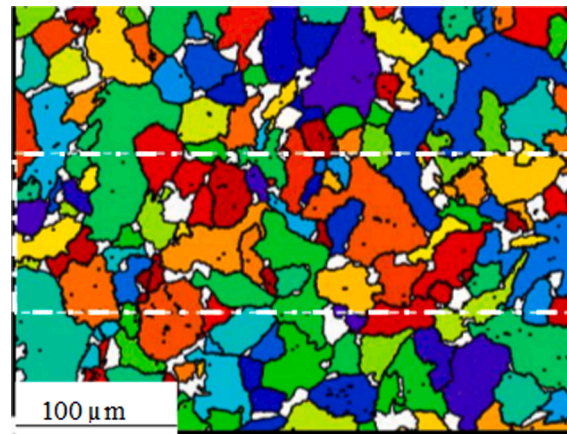**Fig. 4.** Microscopic images of CLs (shown by white arrows) at middle section.

Fig. 5. Reconstructed PAG map for the middle section including the CL (white rectangle) [41].
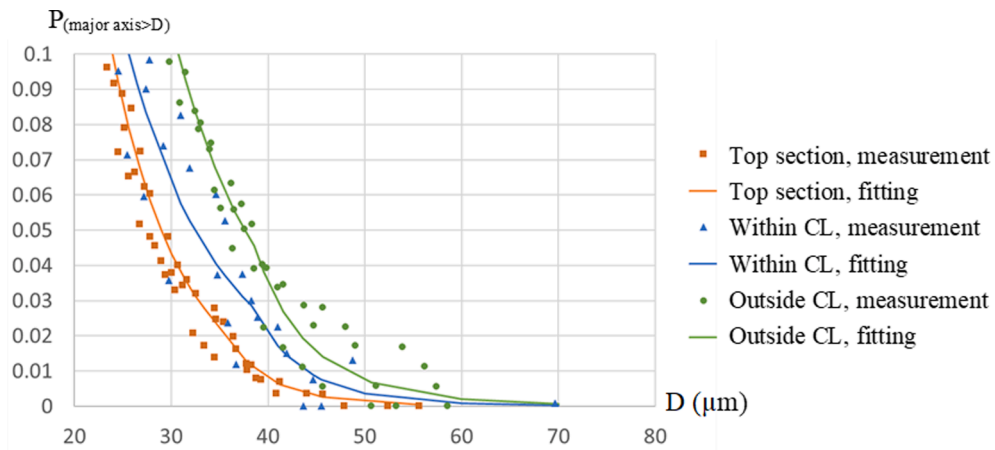

Fig. 6. Distribution of the major axis of PAG.

Table 2
Parameters used to quantify grain size distributions (μ,S in μm, α, β correspond to D in μm).

Values for Top	Values for Middle	
	Outside CLs	Inside CLs
$\mu = 2.50$	$\mu = 2.79$	$\mu = 2.52$
$S = 0.53$	$S = 0.52$	$S = 0.59$
$\alpha = 2.46 \times 10^{17}$	$\alpha = 4.80 \times 10^{9}$	$\alpha = 5.01 \times 10^{10}$
$\beta = 12.24$	$\beta = 6.95$	$\beta = 7.73$

3.3. Inclusions

SEM with Energy-dispersive X-ray spectroscopy (EDS) was used to study morphology and chemical composition of inclusions, while quantification was performed by Keyence optical microscope [40]. Spherical inclusions and second-phase particles were observed through the full thickness, including oxides and nitrides of rather complex chemical composition such as (Mg,Ti)(O,N), (Mg, Al,Ca)(O,N) and (Mg,Al,Ca,Ti)(O,N). In the middle position, in addition to the spherical inclusions, cubic and elongated inclusions were observed. Niobium-rich carbides and nitrides such as (Ti,Nb)(N), (Ti,Nb)(C), Nb(C), and (Nb,Ti)(C,N) are present in the middle position. Fig. 7 shows the statistical distribution of oxides and Nb inclusion sizes measured in top quarter specimens and middle section specimens. For oxides, the difference between these two locations is very slight. For Nb inclusions, the density in the middle section is much higher, and the Nb inclusions tend to have larger length compared to oxide inclusions. Least-square fitting with eq. (3)-(2) is performed on the inclusion size data to obtain the parameters. The parameters of two types of inclusions are listed in Table 3.
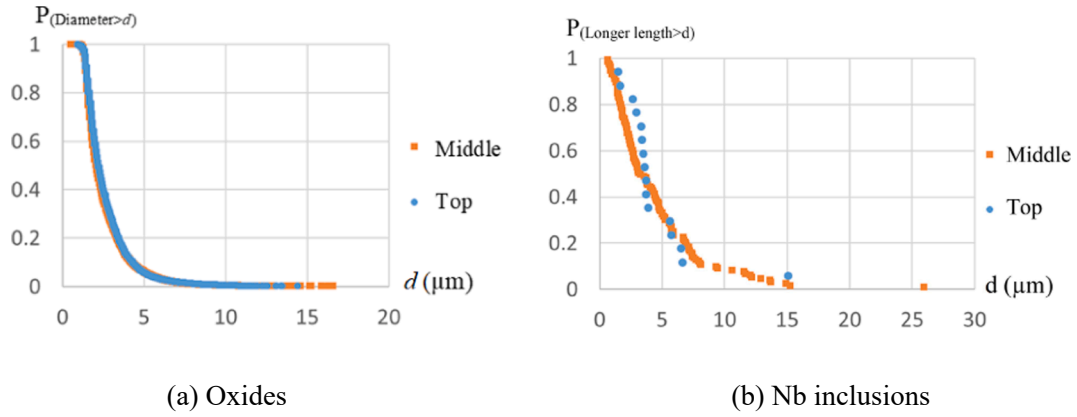
(a) Oxides   (b) Nb inclusions

Fig. 7. Statistical distribution of inclusion size at top quarter and middle section.

Table 3
Parameters quantify inclusion size and density.

Parameters	Values for Top	Values for Middle
Number of oxides per 0.001 mm^3	43	38
Number of Nb inclusions per 0.001 mm^3	1	13
Diameter of oxides (μm)	$\mu = 0.85, S = 0.50$	$\mu = 0.81, S = 0.52$
	$\alpha = 18.32, \beta = 3.57$	$\alpha = 31.64, \beta = 3.86$
Major axis of Nb inclusions (μm)	$\mu = 1.15, S = 0.86$	$\mu = 1.25, S = 0.72$
	$\alpha = NA, \beta = NA*$	$\alpha = 121.93, \beta = 3.07$

* α and β are not applicable to Nb inclusions in the top quarter section because the number of observed Nb inclusions is not enough for the fitting.

$$P(\text{Diameter or major axis} > d) = \min\left\{1 - \text{lognormalCDF}(d, \mu, S), \frac{\alpha}{d^\beta}\right\} \tag{3-2}$$

3.4. Yield properties

Tensile tests were performed [40] according to ISO 6892-3 [42] at −100 °C using cylindrical specimens, in three different orientations relative to the rolling direction: parallel, perpendicular and 45°. All tensile specimens were tested at a deformation rate of
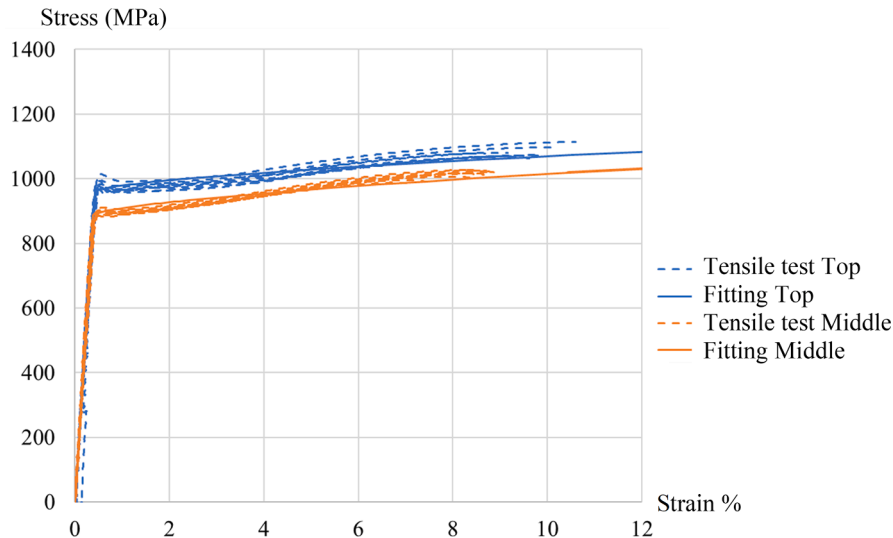

Fig. 8. True stress vs True strain curve of tensile tests and fitting with eq. (3)-(3) (tensile test curves are plotted until the maximum stress).

1.2 mm/s in order to apply similar strain rate conditions as in CTOD specimens. The true-stress vs true-strain curves are present in Fig. 8. Tensile tests of specimens taken from the top and middle sections of the plate indicate that the material at the top section has a higher yield strength and slightly lower degree of hardening. The stress–strain relationship of the steel is characterized by Ludwik's law, which is defined with the flow stress (σ) and the effective plastic strain (ε_p) as:

$$\sigma = \sigma_y + K\varepsilon_p^{n_L}. \tag{3-3}$$

where K and n_L are material parameters. The parameters of Ludwik's law are fitted from tensile tests and the fitted stress–strain curves are shown in Fig. 8. Regarding the effect of orientation, for both thickness positions – top and middle –there is no significant and clear effect of orientation in tensile properties for this material at −100 °C. Therefore, the materials are considered isotropic.

In order to extract the constitutive parameters of the CLs and quantify the variation of local yield parameters in the middle section specimens, nano-indentation measurements have been performed at room temperature [41]. Fig. 9 shows one indentation map where CLs appear. The average hardness values within the CLs are 35% higher than the values outside CLs.

Inverse analysis method proposed by [43] is used to determine the Young's modulus, yield strength and Hollomon hardening exponent from the load-depth curves of the nano-indentation measurements. As expected, little variation of Young's modulus is observed inside and outside CLs. The hardening behaviour of the material is found to be very slight for all indentations, with average value for the Hollomon exponent of 0.006 and standard deviation of 0.032. Therefore, the main distinction in the constitutive parameters is reflected by the yield strength. Table 4 shows the mean value and standard deviation (S) of the yield strength calculated from the locations within and outside CLs in the middle specimen.

The yield strength of the middle section calculated from the nano-indentation test is higher than the value determined from macroscopic tensile tests. This can be explained by the small scale of the indentation (average indentation depth is smaller than 100 nm) and the possibility that the indentations are partially at particles or carbides. Therefore, instead of directly using values in Table 4 as the yield strength for modelling, a relative ratio of the yield strength $\sigma_{y,CL}/\sigma_{y,OutCL} = 2050/1739 = 1.18$ is calculated between the location within and outside CLs and is later used to model the segregation bands.

3.5. Fracture toughness tests

Fracture toughness tests were performed [40] according to the standard ISO 12135 [44] at −100 °C using sub-sized Single Edge Notched Bending (SENB) specimens, with dimensions of 20 mm × 10 mm × 92 mm, crack depth to width ratio a/W of 0.5, 0.25, and 0.1 and on both L-T and T-L orientations (as defined in [44]). All fracture specimens were tested in 3-point bending at a loading rate of 2 mm/s using a MTS servo hydraulic. A summary of the measured crack-tip-opening-displacement (CTOD) values is present in Table 5. The CTOD values for the top section are greater than for the middle and specimens in low-constraint condition exhibit much higher CTOD values than those of high constraint. There is no significant and clear effect of orientation on toughness, and the data of L-T and T-L are mixed for further analysis in this paper.

4. Method

The data sets include deep cracked and shallow cracked specimens taken from the top quarter section and middle section of the S690 QT steel plate. The developed model is firstly applied on the top section specimens to determine the dominant micro-features in the cleavage process and the associated parameters. The model is then applied on the middle section specimens to investigate the
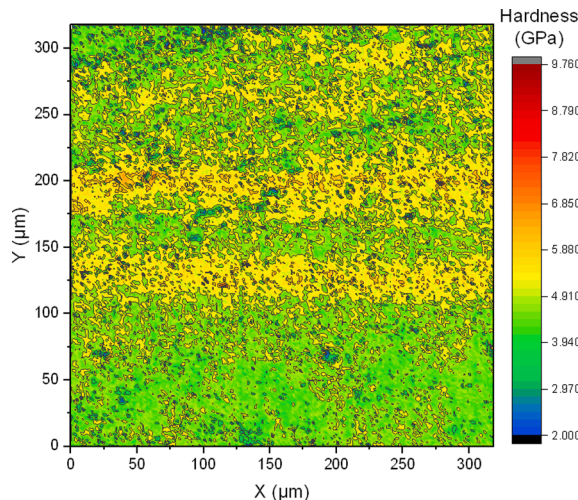

Fig. 9. Hardness map from nano indentations within CLs and outside CLs [41].

Table 4

Yield strength determined by nano-indentation at room temperature.

Locations	Mean value (MPa)	S (MPa)
CLs	2050	425
Outside CLs	1739	336

Table 5

Summary of fracture toughness test results [40].

Constraint		Position	Orientation	Average CTOD [mm]	Number of specimens
High constraint	a/W = 0.5	Top Quarter	T-L	0.048 ± 0.019	10
			L-T	0.036 ± 0.025	4
		Middle	T-L	0.011 ± 0.001	6
			T-L	0.012 ± 0.006	8
Low constraint	a/W = 0.25	Top Quarter	T-L	0.067 ± 0.045	18
	a/W = 0.1	Middle	T-L	0.034 ± 0.031	6
			L-T	0.046 ± 0.018	7

modelling of CLs in cleavage fracture.

4.1. FE model and input parameters

The geometry of the specimen is shown in Fig. 10 and specified in Table 6. For top quarter section specimens, geometry of a/W = 0.5 and a/W = 0.25 are considered as high (deep-cracked) and low (shallow-cracked) constraint conditions, respectively. For middle section specimens, geometry of a/W = 0.5 and a/W = 0.1 are considered as high and low constraint conditions, respectively.

SENB specimens with the geometry specified in Table 6 are modelled in Abaqus 2017. In total, four analyses are performed to consider the variety of initial crack length and material properties. For each analysis, a quarter of the specimen ($L/2 \times B/2 \times W$) is modelled as a 3D deformable solid by using symmetry. The support and load roller are modelled as analytical rigid surfaces. The contact surface between rollers and the specimen is frictionless. Fig. 11 (a) shows the 3D model of a quarter of the specimen and two rollers. Fig. 11 (b) shows the mesh near the crack tip. The initial prefatigued crack tip is modeled as a finite notch that is 0.005 mm in radius. According to algorithm used by [45], this finite notch is small enough to model the near-crack-tip-field for the CTOD value considered in this study. A 20-noded hexahedral element with reduced integration (C3D20R) is used for the mesh. The smallest element near the crack tip has the dimension 0.001 mm × 0.005 mm × 0.067 mm. Displacement control is used to apply a total deflection of 1 mm. A full Newton-Raphson algorithm is used to solve the geometric and material nonlinearity in an implicit method. The stress–strain relationship of the steel is characterized by eq. (3)-(3) and are reported in Table 7.

In addition to yield properties, other parameters need to be predefined for cleavage modelling are $\varepsilon_{plastic,thre}$, V_0, and $\Delta\sigma_H^C$. The values of all the input parameters are summarized in Table 7.

4.2. Macroscopic homogeneous material

In the specimens taken from the top section of the plate, the statistical characteristics of particles and grains do not show spatial inhomogeneity. Due to the homogeneity, cleavage parameters K_{Ia}^{pm}, K_{Ia}^{mm} and σ_H^C can be determined by inverse analysis of the measured CTOD values on high and low constraint specimens.

Using the method described in Section 2, each combination of K_{Ia}^{pm}, K_{Ia}^{mm} and σ_H^C can generate a probability distribution of CTOD for two different constraint levels of specimens. Inverse modeling is performed by iteratively changing these three key parameters until the likelihood is maximized based on the cumulative distribution of all admissible CTOD values for both constraint conditions. The values of K_{Ia}^{pm} and K_{Ia}^{mm} characterize crack arrest by particle/matrix interface and by grain boundary, that may have similar effect on the
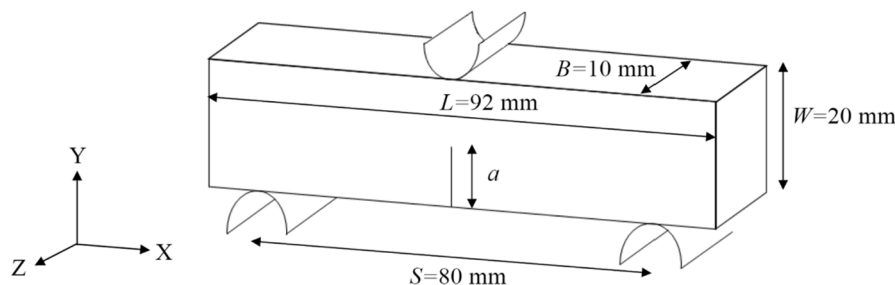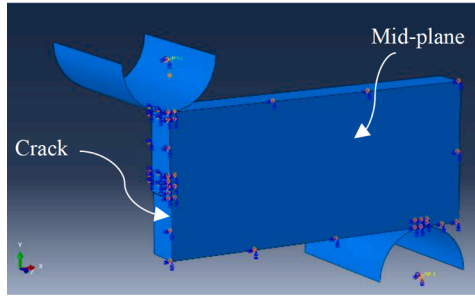

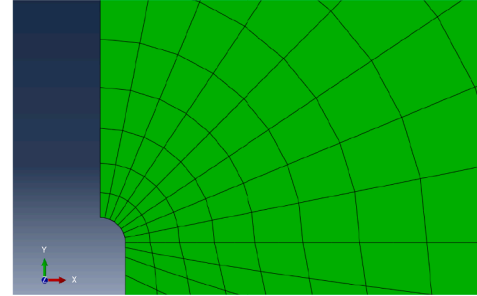**Fig. 10.** Geometry layout of the SENB specimen.

Table 6
Geometric information of the initial crack length.

Constraint	Position in material	Crack length, a (notch length + prefatigued crack length) [mm]
a/W = 0.5	Top quarter section	10 mm (8.6 mm + 1.4 mm)
	Middle section	
a/W = 0.25	Top quarter section	5 mm (3.6 mm + 1.4 mm)
a/W = 0.1	Middle section	2 mm (0.6 mm + 1.4 mm)

(a) Quarter model of the specimen   (b) Mesh near the crack tip

Fig. 11. Finite element model of the three-point bending test.

**Table 7**
Value of the input parameters.

Parameters	Values for Top	Values for Middle	Source
Young's modulus of matrix	219 GPa	236 GPa	Tensile tests
Yield stress (average value)σ_y	961 MPa	888 MPa	
Ludwik hardening parameter: K	489 MPa	593 MPa	
Ludwik hardening exponent: n_L	0.64	0.66	
Threshold plasticity strain $\varepsilon_{plastic.thre}$	10^{-5}	10^{-5}	/
Elementary volume V_0	0.001 mm^3	0.001 mm^3	[45]
Stress concentration factor of spherical inclusion f_α	0.239	0.239	[38]
Scatter of the inclusion fracture strength $\Delta\sigma_H^C$	0.10 GPa	0.10 GPa	/

macroscopic fracture toughness. Based on the microstructural features, the microcrack propagation in cleavage fracture can be either inclusion-size controlled or grain-size controlled [46,47]. The σ_H^C is related to the stress threshold of the cleavage, and is physically not correlated to K_{Ia}^{pm} and K_{Ia}^{mm}.

4.3. Material with macroscopic inhomogeneity

The specimens taken from the middle section of the steel plate contain CLs, which are inhomogeneous through thickness in terms of microstructure and mechanical properties. In Section 3, it shows that the microstructures and yield properties differ between the CLs and areas outside CLs in the middle section specimens.

In this paper, simulation is performed on the middle section specimens with through-thickness crack (representing TL and LT
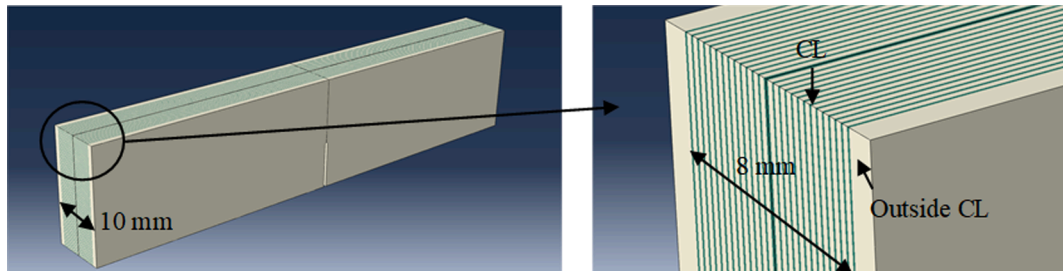
Fig. 12. Modelling of segregation bands as layers in the middle section specimen.

orientation according to [44]). Fig. 12 shows the model of a middle section specimen. The white part is the material that does not contain CLs, and the green layers represent the CLs. The CLs are uniformly distributed over 8 mm across the thickness of the specimen. The thickness of the segregation bands and the spacing between them are 100 μm and 200 μm, respectively.

In Section 3, the characterization of materials suggests three possible distinctions of the segregation bands that can influence the cleavage behavior: the yield strength, the grain size, and the distribution (spatial, size and type) of inclusions. The yield strength difference influences the tensile stress distribution through the thickness, the grain size difference is related to probability of the crack propagation, and the inclusion difference can be reflected by cleavage parameters and inclusion density. While the yield strength difference and the grain size difference are determined explicitly from macroscopic and microscopic measurements, it is questionable whether the cleavage parameters within CLs can be transferred outside CLs, and whether the detrimental effect of brittle inclusions can be homogenized outside CLs. In order to investigate the possible difference in cleavage parameters and the effect on cleavage toughness, two approaches listed in Table 8 are compared within the proposed model.

A "Yield and grain size variation method" is firstly applied on the material. The yield strength and the grain size are considered as different inside and outside the CLs. The volume averaged yield strength of the specimen maintains the value as determined from tensile tests. The yield strength inside and outside the CLs is modified to the ratio calculated from nano-indentation measurements. As a result, yield strength inside CLs $\sigma_{y,CL} = 1.113\sigma_{y,tensile}$ and yield strength outside CLs $\sigma_{y,OutCL} = 0.944\sigma_{y,tensile}$. The same set of cleavage parameters (K_{Ia}^{mm}, σ_H^C) is assumed inside and outside CLs and is fitted from the measured CTOD values. Inclusions are assumed to be uniformly distributed in the middle section. The middle section specimens are assumed as a material that has different cleavage parameters from the top section specimens and the cleavage parameters are homogeneous through the thickness.

In a "Cleavage variation method", the aggregation of Nb inclusions in the CLs is considered by assuming the cleavage parameters are different within and outside CLs, and the Nb inclusions are only distributed in the CLs. The yield strength, the grain size are considered different inside and outside of the CLs, as in the "Yield and grain size variation method". In this approach, the segregation bands are considered as the main features that are different between the middle section specimens and the top section material. The material outside CLs is assumed to have the same value of cleavage parameters as at top section.

5. Results

5.1. Macroscopic homogeneous material

The cleavage parameters are fitted with maximum likelihood method from toughness data measured in two constraint conditions. A non-uniqueness situation occurs when the inverse modelling find several combinations of K_{Ia}^{pm} and K_{Ia}^{mm} that can produce good fits. Fig. 13 shows several sets of K_{Ia}^{pm} and K_{Ia}^{mm} are found to generate the same CTOD distributions that fit the experiments of the reference steel, when inverse modelling is performed with "initial guess of parameters" varying in a wide range. The dashed line in Fig. 13 are formed by connecting the fitted [K_{Ia}^{pm}, K_{Ia}^{mm}] combinations.

The non-uniqueness of K_{Ia}^{pm} and K_{Ia}^{mm} can be explained analytically. Both K_{Ia}^{pm} and K_{Ia}^{mm} relate local tensile stress $\sigma_{1,matrix}$ to a probability of microcrack propagation, via eq. (2)-(3), 2–4 respectively. The probability of a microcrack propagating across inclusion/grain interface and grain boundary is:

$$p = p_1(\text{inclusionsize} > d_c) \times p_2(\text{grainsize} > D_c) \tag{5-1}$$

If $p_1 \ll 1$ and $p_2 \ll 1$, it means that both the inclusion/grain interface and the grain boundary act as the barrier to crack propagation. It is found that when $p_1 \ll 1$ and $p_2 \ll 1$, eqs. (3)-(1) and 3–2 can be characterized by power-law equations, and 5–1 can be written as

$$p = \frac{\alpha_1}{d_c^{\beta_1}} \times \frac{\alpha_2}{D_c^{\beta_2}} = \frac{\alpha_1}{\left(K^{pm}/\sigma_{1,matrix}\right)^{2\beta_1}} \times \frac{\alpha_2}{\left(K^{mm}/\sigma_{1,matrix}\right)^{2\beta_2}} \tag{5-2}$$

When eq. (5)-(2) holds, several sets of K_{Ia}^{pm} and K_{Ia}^{mm} result in the same value of p, and neither of the two parameters can be uniquely determined from the probability distribution of CTOD. However, an unique value of K_{Ia}^{pm} or K_{Ia}^{mm} can be determined by evaluating the sensitivity of the simulated toughness to the change in the fitted parameters.

Fig. 13 evaluates the sensitivity of the median value of the simulated CTOD (CTOD$_{med}$) to the change of K_{Ia}^{pm}. Seven points having values of K_{Ia}^{pm} and K_{Ia}^{mm} on the dashed line are evaluated. The change in CTOD$_{med}$ (ΔCTOD$_{med}$) is calculated for a small change in K_{Ia}^{pm} ($\Delta K_{Ia}^{pm} = 0.1$ MPa$\sqrt{\text{m}}$) of each points. The sensitivity is expressed as ΔCTOD$_{med}/\Delta K_{Ia}^{pm}$ and is plotted along the vertical axis in Fig. 13. It is found that, ΔCTOD$_{med}/\Delta K_{Ia}^{pm}$ starts to increase when $K_{Ia}^{pm} > 3.0$ MPa$\sqrt{\text{m}}$. It is also found, when $K_{Ia}^{pm} > 3.0$ MPa$\sqrt{\text{m}}$, the dashed line

Table 8
Approaches with varied considerations of CLs.

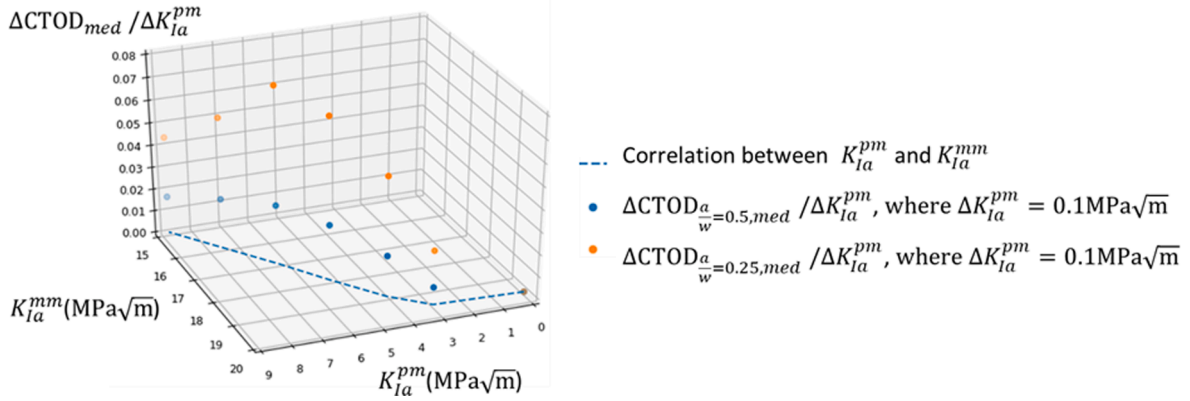| Approach	Parameter different inside and outside of segregation band			
	Inclusion density	Grain size	Yield strength	K_{Ia}^{mm} and σ_H^C
Yield and grain size variation	No	Yes	Yes	No
Cleavage variation	Yes	Yes	Yes	Yes

Fig. 13. Sensitivity of the median predicted CTOD value to K_{Ia}^{pm}.

coincides with eq. (5)-(2). It means $p_1 \ll 1$ and $p_2 \ll 1$ holds for $K_{Ia}^{pm} > 3.0$ MPa$\sqrt{\mathrm{m}}$.

However, when $K_{Ia}^{pm} < 3.0$ MPa$\sqrt{\mathrm{m}}$, it is shown that $\Delta CTOD_{med}/\Delta K_{Ia}^{pm}$ is close to zero, which means the simulated fracture toughness is not sensitive to the change of K_{Ia}^{pm}. It indicates p_1 cannot be approximated by a power law equation and eq. (5)-(2) does not hold when K_{Ia}^{pm} is low (< 3.0 MPa$\sqrt{\mathrm{m}}$ for the reference material). In this case, inclusion/grain interface is not a barrier to crack propagation, and as the only controlling parameter, K_{Ia}^{mm} can be uniquely determined.

The threshold value of K_{Ia}^{pm} for the non-uniqueness depends on the microstructure of the steel. For the reference steel, FEA shows the $\sigma_{1,matrix}$ is around 2000–2500 MPa. The critical inclusion size corresponding to $K_{Ia}^{pm} = 3$ MPa$\sqrt{\mathrm{m}}$ is 1.44–2.25 μm according to eq. (2)-(3). Fig. 7 shows that the brittle inclusions have a relatively large dimension compared to 1.44–2.25 μm, and the nucleated microcracks are in sizes that can automatically propagate into the neighbouring or parent grain if $K_{Ia}^{pm} < 3.0$ MPa$\sqrt{\mathrm{m}}$.

Examination of fracture surfaces was performed using SEM to characterize the mode of failure and to locate and identify microstructural features that may have triggered cleavage [40]. Larger inclusions have been observed on the fracture surface, while Fig. 14 shows the smallest inclusions that are identified as local cleavage fracture initiation sites. The micro-cracks of the shown inclusion size are able to propagate across the inclusion/matrix interface and form cleavage facets among neighboring grains. The inclusions are of sizes 1.22 (± 0.08) μm and 1.27 (± 0.10) μm respectively, below the value of 1.44–2.25 μm. It shows that in the reference steel, the K_{Ia}^{pm} should below 3.0 MPa$\sqrt{\mathrm{m}}$, and the dominant barrier to micro-crack propagation is the grain boundary.

Similar sensitivity studies were performed for all the other parameters. It was found that σ_H^C ranged from 1.00 GPa to 3.50 GPa is another controlling parameter independent of K_{Ia}^{pm} and K_{Ia}^{mm}, while $\varepsilon_{plastic,thre}$, V$_0$, and $\Delta\sigma_H^C$ show little impact with their predefined values in Table 7. Fig. 15 shows the sensitivity of the simulated CTOD to the values of K_{Ia}^{mm} and σ_H^C. While the simulated toughness monotonically increases with K_{Ia}^{mm}, it shows non-monotonicity for σ_H^C. Determination of σ_H^C with only one constraint condition may lead to non-uniqueness.

With the recognition that the micro-crack propagation is grain-size controlled, the probability of inclusion-sized micro-crack propagation is set to be 1. Maximum likelihood fitting is performed with this modification, and the values of K_{Ia}^{mm} and σ_H^C are deter-
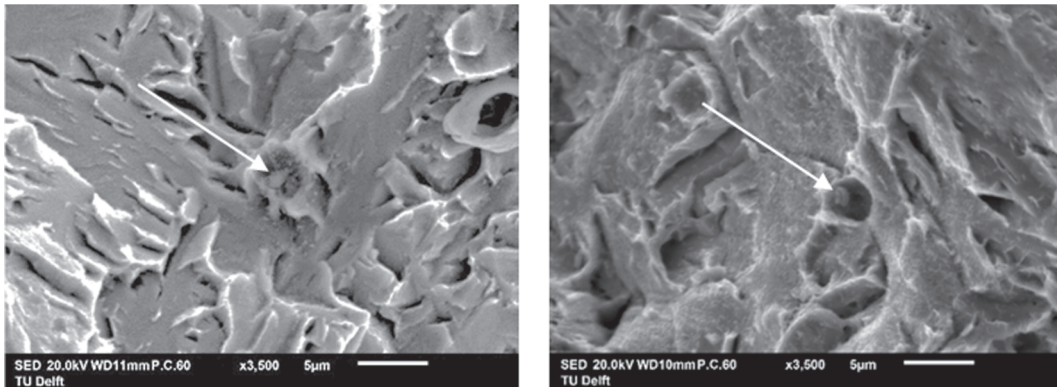
(a) High constraint, Top quarter   (b) Low constraint, Top quarter

Fig. 14. Inclusions (indicated by white arrows) acting as initiation site of the fractured specimens.

(a) Sensitivity to K_{Ia}^{mm} when $\sigma_H^C = 2.71$ GPa   (b) Sensitivity to σ_H^C when $K_{Ia}^{mm} = 19.7$ MPa$\sqrt{m}$
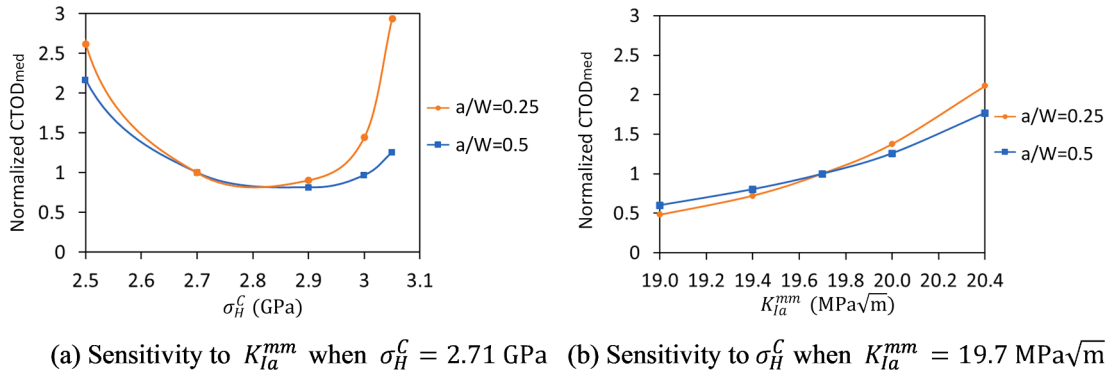
Fig. 15. Sensitivity of the simulated CTOD to cleavage parameters (present as the simulated CTOD corresponds to 50% fracture probability normalized by the ones simulated by the best-fit parameters).

mined as $K_{Ia}^{mm} = 19.7$MPa$\sqrt{m}$ and $\sigma_H^C = 2.71$ GPa. Fig. 16 shows the cleavage probability curve reproduced by the determined cleavage parameters for the top section specimens, which matches the experimental results well for high constraint specimens and low constraint specimens.

5.2. Material with macroscopic inhomogeneity

For "Yield and grain size variation method", the maximum likelihood fitting results in $K_{Ia}^{mm} = 20.0$MPa$\sqrt{m}$ and $\sigma_H^C = 2.03$ GPa. For "Cleavage variation method", K_{Ia}^{mm} within CLs and σ_H^C of Nb inclusions are fitted with maximum likelihood fitting as $K_{Ia}^{mm} = 19.0$MPa$\sqrt{m}$ and $\sigma_H^C = 2.21$ GPa. Table 9 summarized the value of cleavage parameters determined for both top and middle sections. Consequently, Fig. 17 shows the curves produced by the fitted parameters. The two approaches both extract cleavage parameters from maximum likelihood fitting and result in a similar level of fitting quality. However, the varying values of cleavage parameters indicate that the effect of segregation bands is differently represented in these two approaches, which will be further compared in Section 5.3.

5.3. Effect of volume fraction, yield stress, and spacing of segregation bands on fracture toughness

To further evaluate the effect of segregation bands on cleavage toughness and to investigate the more physically-based approach of modelling the through thickness inhomogeneity, a sensitivity study is performed with the two methods proposed in Section 4 on virtual materials assuming various volume fraction, yield strength, and spacing of CLs. The fitted K_{Ia}^{mm} and σ_H^C from "Yield and grain size variation method" and "Cleavage variation method" are used to predict the fracture probability.

(1) Volume fraction of CLs

CLs show two opposite effects on cleavage fracture. The finer grains prevent crack propagation across grain boundaries, while the stress concentration promotes inclusion cracking and micro-crack propagating. The ratio between volume of CLs (V_{CL}) and the total volume including CLs ($V_{CL} + V_{OutCL}$), is defined as the volume fraction of CLs $f_{CL} = \frac{V_{CL}}{V_{CL}+V_{OutCL}}$. The reference analysis in Section 4 corresponds to $f_{CL} = 1/3$. For a virtual material, assuming the properties inside CLs and outside CLs as same as for the reference analysis in Section 4, an increased f_{CL} increases the local tensile stress but decreases the grain size. When the cleavage parameters are the same inside and outside CLs, the total effect on fracture toughness depends on the relationship between the yield stress and the grain size. If, in relation to the change of grain size, there is a more significant increase in yield stress, the existence of CLs is detrimental to toughness. Otherwise, the effect of finer grains is more pronounced and the CLs shows no detrimental influences.

Fig. 18 shows fracture toughness predicted by the "Yield and grain size variation method" is not sensitive to the volume fraction of CLs, which indicates that for the investigated material, the effects of higher yield stress and finer grain size inside the CLs approximately cancel each other.

However, with the "Cleavage variation method", the toughness is more sensitive to the existence of CLs. The tensile stress in the middle section would not be high enough to initiate crack in oxides. CLs contain Nb inclusions that have lower fracture strength and are more prone to cracking, and the toughness will be much decreased as the volume fraction of CLs increases.

(2) Yield stress of segregation bands

Hardness tests showed that the CLs have a higher yield stress. The ratio between the yield stress inside and outside CLs $f_\sigma = \sigma_{y,CL}/\sigma_{y,outCL}$ represents the stress concentration effect brought by the CLs. The reference analysis in Section 4 has $f_\sigma = 1.18$. While the average yield stress remains constant, an increased ratio f_σ results in a higher stress inside the CLs, but a lower stress outside.

Fig. 19 shows the sensitivity of the fracture toughness predicted by the two methods to the change of f_σ. For the "Yield and grain size
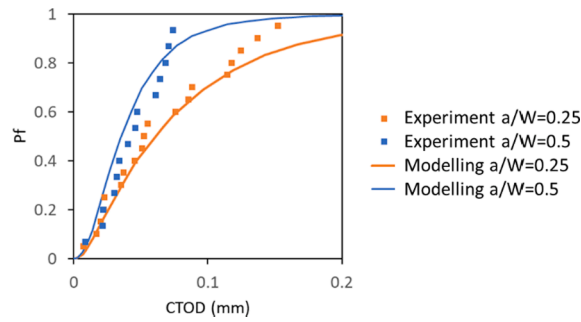
Fig. 16. Cleavage probability calculation of top section specimens based on fitted parameters.

Table 9

Summary of cleavage parameters determined for both top and middle sections.

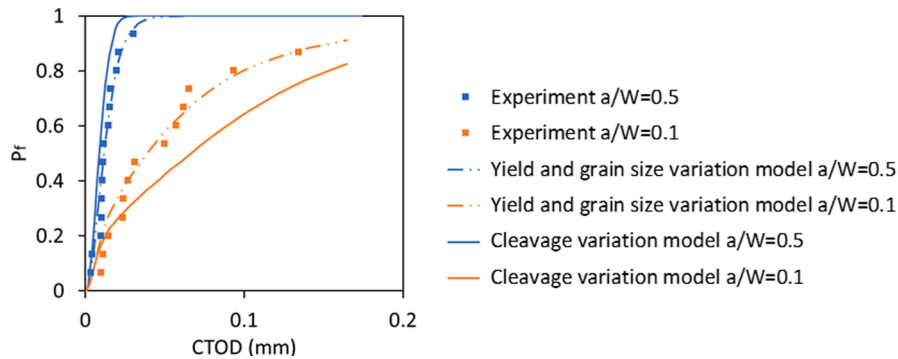| Parameters	Values for Top	Values for Middle (Cleavage variation method)			Values for Middle (Yield and grain size variation method)
		CL		Out CL	
K_{Ia}^{mm}	19.7 MPa$\sqrt{\text{m}}$	19.0 MPa$\sqrt{\text{m}}$		19.7 MPa$\sqrt{\text{m}}$	20.0 MPa$\sqrt{\text{m}}$
σ_H^C with $\Delta\sigma_H^C = 100$ MPa	2.71 GPa	Nb inclusion	2.21 GPa	2.21 GPa	2.03 GPa
		Oxides	2.71 GPa	2.71 GPa	

Fig. 17. Cleavage probability calculation of middle section specimens and corresponding fitted parameter from "Cleavage variation method"

variation method", the materials inside and outside CLs both contribute to the cleavage fracture. The increased stress inside CLs raise the fracture probability and the reduced stress outside CLs decrease the fracture probability. Consequently, little influence is reflected by varying the f_σ. For the "Cleavage variation method", the cleavage fracture is initiated by Nb inclusions distributed within CLs. The material outside CLs has little contribution. The increase of yield stress inside CLs leads to a lower level of fracture toughness, while the decrease of yield stress outside CLs has little effect. As a result, the fracture toughness predicted by the "Cleavage variation method" is reduced by a higher f_σ.

(3) Spacing of the segregation bands

In previous sections, the CLs are uniformly modelled over 8 mm across the thickness of the specimen, and the space among bands is 200 µm. Fig. 20 shows an extreme condition where the same volume of CLs are aggregated together instead of uniformly distributed, that the space among the modelled bands is zero. In Fig. 20, the CLs are located at the mid-plane. The aggregated bands increase the stress level in CLs by giving more constraint on the deformation. Meanwhile, the aggregated bands reduce the stress level outside the CLs, as the constraint of deformation is reduced.

Fig. 21 shows CTOD predictions of the case in Fig. 20 based on "Yield and grain size variation method" and "Cleavage variation method". For the "Yield and grain size variation method", the aggregation of segregation bands leads to opposite effects on the predicted fracture toughness, and the fracture toughness is not sensitive to the change in band spacing and band location. For the "Cleavage variation method", the tensile stress within the CLs is dominant in the cleavage behaviour. The aggregated bands leads to a lower level of fracture toughness.

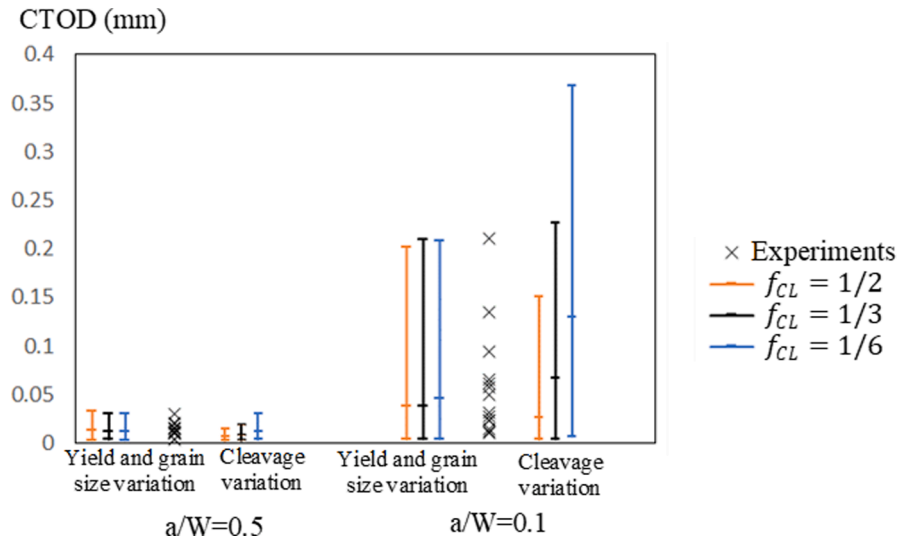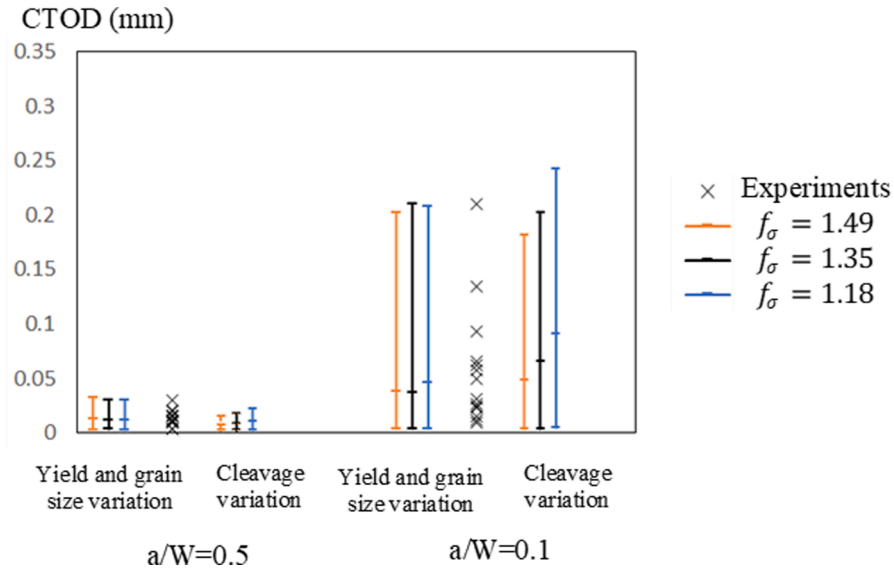**Fig. 18.** Cleavage prediction of various $f_{CL} = \frac{V_{CL}}{V_{CL} + V_{OutCL}}$.

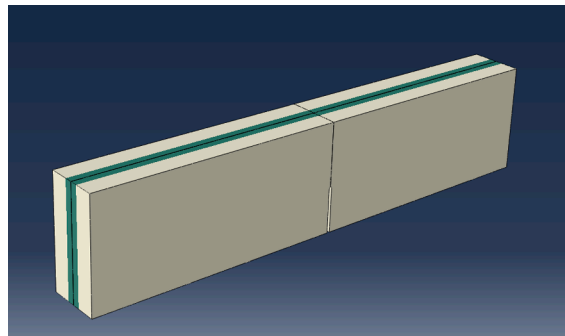**Fig. 19.** Cleavage prediction of various $f_{\sigma} = \sigma_{y,CL}/\sigma_{y,outCL}$.

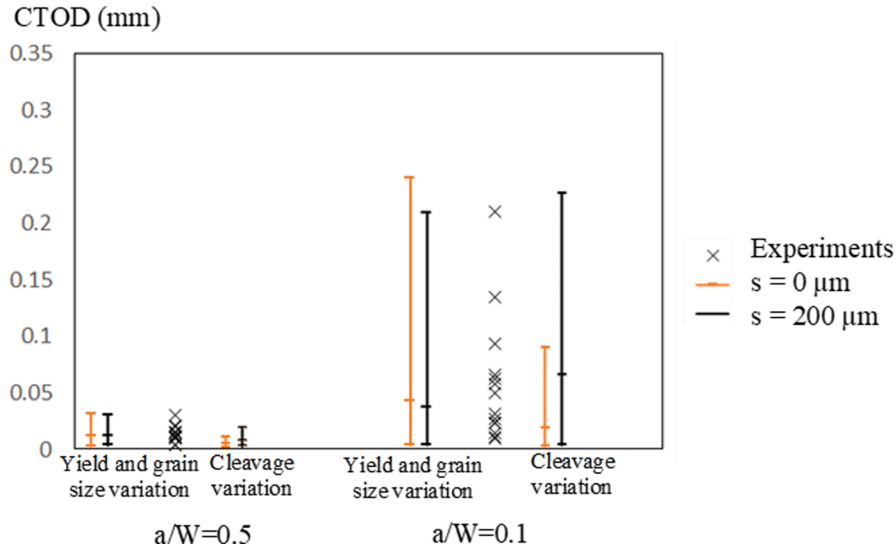**Fig. 20.** Aggregated segregation bands (zero space between bands).

Fig. 21. Cleavage prediction of uniformly distributed (s = 200 μm) and aggregated (s = 0 μm) CLs.

6. Discussion

The microstructural-informed statistical model presented in this paper is developed from multi-barrier theory of cleavage fracture, and it predicts the cleavage fracture toughness of steels from the microstructural information and tensile properties. The method has been applied on an 80 mm thick S690 QT steel plate, and the capability to characterize the scatter of the macroscopic fracture toughness for deep and shallow cracked geometries is verified. The investigated material shows through thickness inhomogeneity and the model is able to reflect the microstructural changes on fracture toughness.

6.1. Determination of cleavage parameters

The model contains three cleavage parameters K_{Ia}^{pm}, K_{Ia}^{mm} and σ_H^C, that correspond to three critical events in the cleavage process. For each combination of the three cleavage parameters, the model predicts the fracture probability at a global load. The σ_H^C is related to the stress threshold of the cleavage, and is physically not correlated to K_{Ia}^{pm} and K_{Ia}^{mm}. The values of K_{Ia}^{pm} and K_{Ia}^{mm} characterize crack arrest by particle/matrix interface and by grain boundary, that may have similar effect on the macroscopic fracture toughness. When there is a distinct difference in the sensitivity of predicted toughness to the change of K_{Ia}^{pm} and K_{Ia}^{mm}, as for the sample steel in this paper, the controlling factor can be judged. In other cases, either microscopic measurements need to be performed, or another set of macroscopic measurements should be performed for a varied microstructure to determine the unique values of K_{Ia}^{pm} and K_{Ia}^{mm}. The cleavage parameters need to be determined by combinations of macroscopic mechanical testing and microstructural characterizations, and can be applied on toughness prediction in structural components where gradient changes of microstructures are expected (e.g. HAZ).

The current model calculates the fracture probability in the volume that has plastic deformation. This is based on the assumption that plasticity near hard particles is necessary to initiate cracks in them. For the investigated high strength steel, the fitted σ_H^C is higher than 2.00 GPa. The first principal stress of the material at local yielding is less than 1.70 GPa for deep cracked specimens, which supports the assumption. Analysis without the plastic strain criterion also shows there is little influence by applying a stress threshold, instead.

The initial crack tip is modelled as stress-free, while in reality there could be residual compressive stress from pre-fatigue. The maximum fatigue precracking load is determined according to [44], that $K_{I,max} = 25 MPa\sqrt{m}$. 96% of all the fractured specimens have $K_{I,c} > 50 MPa\sqrt{m}$, and the remaining two specimens have the lowest $K_{I,c} = 42 MPa\sqrt{m}$. Since the failure loads are much higher than the fatigue load, the effect of residual stress resulted from pre-fatigue on the cleavage initiation of the tested specimens can be assumed as minor.

Constraint conditions influence cleavage fracture due to the local state of tensile stress and the plastic deformation. In previous local approach models, such as Beremin method, Weibull stress is used to quantify the effect of local tensile stress and a threshold of Weibull stress has been proposed by [48,49], to improve the agreement between high and low constraint conditions. In [17,50], plastic strain based terms are used to correct Weibull stress to reflect the effect of plastic strain on particle cracking, which further improve the transferability of cleavage parameters among various geometries. In comparison, the present model uses parameter K_{Ia}^{mm} to represent the effect of local tensile stress on crack propagation, and parameter σ_H^C to set a threshold of tensile stress. The effect of plastic deformation on particle cracking is reflected by eqs. (2)-(1), 2–2. The present model is applied on SENB specimens with different crack depths (a/W = 0.1, 0.25, 0.5), and shows the ability to simulate toughness for both high and low constraint conditions. When

represented by T-stress/nominal stress (as defined in [51]) the present geometries cover a range of [-0.46, 0.25], and when represented by stress triaxiality at the crack tip (as defined in [52]) the present geometries cover a range of [1.80, 2.33]. Both values are typical for cracked specimens. It is reasonable to assume the determined cleavage parameters can be transferrable to other geometries (such as pre-cracked CT specimens) where the fracture is pure cleavage. However, for uncracked geometries (such as round notched bars) that show interactions of cleavage and ductile failure due to lower constraint, the cleavage parameters will be varied.

6.2. Simulation of segregation bands

In this paper, two strategies of modelling CLs are compared. The main difference of the two methods is whether to assume the material containing CLs to have homogenous cleavage parameters, or assume the cleavage parameters inside CLs to be distinctive. Although the two methods both show satisfactory correlation with the experiments on S690 QT steel, they result in different reflection of the CLs on fracture toughness predicted for virtual materials. CLs have finer grains preventing crack propagation, and higher yield strength promoting inclusion cracking and micro-crack propagating. Clusters of Nb inclusions have been observed within the CLs as shown in Fig. 22 (a). Nb inclusions were also identified as a trigger in the cleavage fracture. Fig. 22 (b) and (c) show that a cubic Nb-rich inclusion large in size triggered the fracture process of a middle section specimen. From fracture surface analysis, initiation sites can be identified in nine of the middle section specimens, and seven of them have initiation sites identified as Nb inclusions.

With the "Yield and grain size variation method", the effects of higher yield stress and finer grain size inside the CLs approximately cancel each other. The predicted fracture toughness is not sensitive to changes in CLs. In the case of "Cleavage variation method", the fracture toughness is predicted to be reduced for higher volume fraction of CLs, higher yield strength ratio of CLs, and aggregation of CLs. It proves that the detrimental effect of CLs is not only associated with grain structures and tensile properties, but strongly related to the microstructural toughness parameters, especially the cleavage strength of inclusions. As a comparison, in previous literature studying CLs [31], brittle TiN particles appears with similar frequency at the top and middle sections of a steel plate, and a profound refinement of the local grain size at the centreline is observed. The refinement of grain size compensates for the harder microstructure in CLs, and the heterogeneous material containing CLs does not show detrimental effect to toughness properties.

In the two methods, the value of fracture strength of inclusions σ_H^C cannot be transferred from middle section to the top quarter section, while the values of K_{Ia}^{mm} are relatively stable through the thickness. When microstructural cleavage parameters are assumed to be transferred from the centreline to outside the centreline, the detrimental effect of CLs is not properly reflected. It indicates that the cleavage parameter associated to a local brittle microstructure should not be homogenized outside the local brittle zone and a "Cleavage variation method" is required to better capture the influence of the local brittle zone on macroscopic toughness.

Bimodal local approach methods were applied to model the effect of inhomogeneities on fracture toughness [32,33], which assume the cleavage properties of local brittle zones can be represented by macroscopically homogeneous material at tens-of-millimeter scale. The Bimodal methods can successfully describe the statistical characteristics of a mixed data sets including several different materials, but are not able to relate the cleavage properties to microstructural features. Multi-barrier models that incorporate microstructural information are capable of capturing the micron-level features. However, such models were not applied to simulate CLs and rarely consider particle deactivations. For example, the same material studied in the present paper has been simulated in [38] with a multi-barrier method proposed by [36], without the modelling of CLs and the consideration of particle deactivations. The fitted parameters in [38] reflect similar conclusion as the "Yield and grain size variation method" used in the present paper, indicating a significantly lower cleavage stress of hard particles at the middle section, but did not provide insight into the specific effect of higher yield strength, finer grain size and brittle inclusions.

7. Conclusions

A microstructure-informed statistical method is proposed in this paper to model cleavage fracture in high strength steels containing through thickness inhomogeneities. The model is developed from a multi-barrier theory with particular intention to include the effect

(a)　　　　　　　　(b)　　　　　　　　(c)
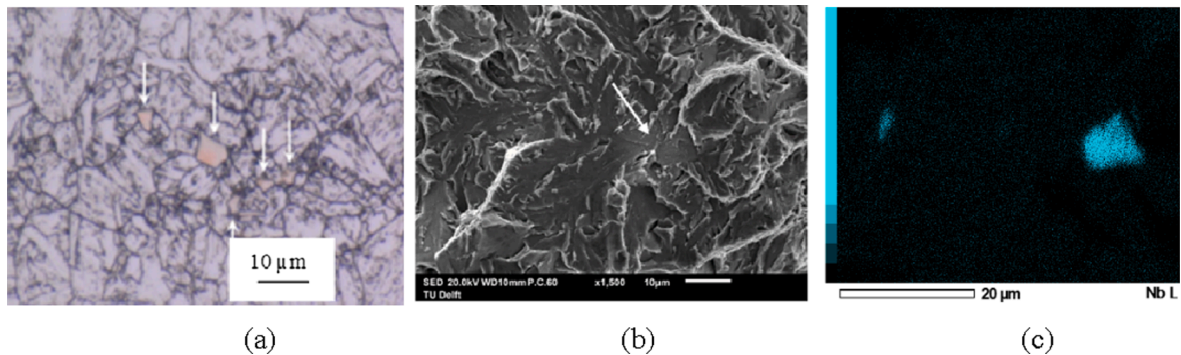
Fig. 22. Images showing (a) inclusions present in CLs (indicated by arrows) for the middle section. (b) Nb-rich inclusion (indicated by white arrow) acting as cleavage initiation site (c) Nb maps of the inclusion at the fracture initiation site in (b) [40].

of plastic strain and deactivation of hard inclusions. Examples of top quarter specimens and middle section specimens taken from the S690 QT steel plate fractured at $-100\ °C$ are used to validate the modelling method. Centreline segregation bands (CLs) appear in the middle section specimens, containing smaller grains and elongated inclusion clusters. In this paper, the statistical microstructural parameters and local yield properties of CLs are extracted from previous data in [40,41], and two modelling approaches are compared to discuss the effect of CLs in cleavage modelling. A sensitivity study has been performed to explore the influence of volume fractions, yield strength, and spacing of CLs. The following conclusions are highlighted for modelling cleavage fracture using the present model:

- Grain boundary rather than particle/matrix interface is identified as the barrier to microcrack propagation for the S690 QT, as the majority of hard inclusions are in size above micrometer.
- Existence of CLs has two opposite effects on cleavage fracture. The finer grains prevent crack propagation across grain boundaries, while the stress concentration promotes inclusion cracking and crack propagating.
- With "Yield and grain size variation method" the effects of higher yield stress and finer grain size inside the CLs approximately cancel each other. The predicted fracture toughness is therefore not sensitive to changes in CLs.
- In the case of "Cleavage variation method", the fracture stress of oxides is higher than the stress level outside CLs. The CLs of the sample steel contain Nb inclusions that have lower fracture strength and characterize the cleavage behaviour.
- The "Cleavage variation method" shows that predicted fracture toughness is sensitive to the change of CLs. The toughness is predicted to be reduced for higher volume fraction, higher yield strength ratio, and aggregation of CLs.

The conclusions lead to a general suggestion that the cleavage parameter associated to a local brittle microstructure should not be homogenized outside the local brittle zone and a "Cleavage variation method" is required to better capture the influence of the local brittle zone on macroscopic toughness. The present methodology can quantitively capture the cooperating of complex microstructures in cleavage and can be used to facilitate the trade-off between various microstructural parameters in toughness control.

In addition, the present modelling approach has the following limitations that could be further investigated:

- The current model does not consider local variations of cleavage parameters at microscale. It does not account for cleavage parameters of ductile inclusions.
- The current model is verified for through thickness pre-fatigued crack, while surface crack and uncracked notch are not investigated in this paper.
- The current model does not include residual stress in CLs and around inclusions.

While the present paper focus on simulation method of through thickness inhomogeneities, a follow-up research is prepared to further investigate the transferability of cleavage parameters by applying the present method on different types of steels and specimen geometries. Another intended future research is to perform isoparametric changes of the microstructures by heat treatment to provide more quantitative comparisons from experiments.

CRediT authorship contribution statement

Quanxin Jiang: Writing – original draft, Conceptualization, Data curation, Visualization, Investigation, Validation, Formal analysis, Methodology. **V.M. Bertolo:** Writing – review & editing, Resources, Methodology, Data curation, Conceptualization. **V.A. Popovich:** Writing – review & editing, Supervision, Project administration, Conceptualization. **J. Sietsma:** Writing – review & editing, Supervision, Conceptualization. **Carey L. Walters:** Writing – review & editing, Validation, Supervision, Conceptualization.

Declaration of Competing Interest

The authors declare that they have no known competing financial interests or personal relationships that could have appeared to influence the work reported in this paper.

Acknowledgement

References

[1] EN 1011, CEN. Welding – Recommendations for welding of metallic materials; 2009.
[2] Miyata T, Yang RC, Otsuka A, Haze T, Ahira S. Cleavage fracture of steels with fine grained ferrite, coarse grained bainitic and martensitic. In: Advances in fracture research proceeding of the seventh international conference of fracture; 1989. p. 2563–71.
[3] Lee S, Kim S, Hwang B, Lee BS, Lee CG. Effect of carbide distribution on the fracture toughness in the transition temperature region of an SA 508 steel. Acta Mater 2002;50(19):4755–62.
[4] Zhou MW, Yu H. Effects of precipitates and inclusions on the fracture toughness of hot rolling X70 pipeline steel plates. Int J Miner Metall Mater 2012;19(9): 805–11.
[5] Li X, Ma X, Subramanian SV, Shang C, Misra RDK. Influence of prior austenite grain size on martensite-austenite constituent and toughness in the heat affected zone of 700MPa high strength linepipe steel. Mater Sci Engng, A 2014;616:141–7.

[6] Trampus P. Micro structural aspects of unstable crack propagation in ferritic steels. Mater Sci Forum 2007;537–538:465–72.
[7] Curry DA, Knott JF. Effects of microstructure on cleavage fracture stress in steel. Metal Sci 1978;12(11):511–4.
[8] Ray A, Paul SK, Jha S. Effect of Inclusions and Microstructural Characteristics on the Mechanical Properties and Fracture Behavior of a High- Strength Low-Alloy Steel. J Mater Engng Perform 1995;4(6):679–88.
[9] Di Schino A, Guarnaschelli C. Microstructure and Cleavage Resistance of High Strength Steels. Mater Sci Forum 2010;638–642:3188–93.
[10] Armstrong RW. Material grain size and crack size influences on cleavage fracturing. Philos Trans Roy Soc A: Math Phys Engng Sci 2015;373(2038):20140474.
[11] Jia T, Zhou Y, Jia X, Wang Z. Effects of microstructure on CVN impact toughness in thermomechanically processed high strength microalloyed steel. Metall Mater Trans A 2017;48(2):685–96.
[12] Pineau A, Benzerga AA, Pardoen T. Failure of metals I: Brittle and ductile fracture. Acta Mater 2016;107:424–83.
[13] Beremin FM, Pineau A, Mudry F, Devaux J-C, D'Escatha Y, Ledermann P. A local criterion for cleavage fracture of a nuclear pressure vessel steel. Metall Trans A 1983;14(11):2277–87.
[14] Wallin K, Saario T, Törrönen K. Statistical model for carbide induced brittle fracture in steel. Metal Sci 1984;18(1):13–6.
[15] Chen JH, Wang GZ, Wang HJ. A statistical model for cleavage fracture of low alloy steel. Acta Metall 1996;44(10):3979–89.
[16] Gao X, Ruggieri C, Dodds RH. Calibration of Weibull stress parameters using fracture toughness data. Int J Fract 1998;92(2):175–200.
[17] Bernauer G, Brocks W, Schmitt W. Modifications of the Beremin model for cleavage fracture in the transition region of a ferritic steel. Engng Fract Mech 1999;64(3):305–25.
[18] Bordet SR, Karstensen AD, Knowles DM, Wiesner CS. A new statistical local criterion for cleavage fracture in structural steel. Part I: Model presentation. Engng Fract Mech 2005;72:435–52.
[19] Gao X, Zhang G, Srivatsan TS. Prediction of cleavage fracture in ferritic steels: A modified Weibull stress model. Mater Sci Engng, A 2005;394(1–2):210–9.
[20] Wallin K, Laukkanen A. New developments of the Wallin, Saario, Törrönen cleavage fracture model. Engng Fract Mech 2008;75(11):3367–77.
[21] Shibanuma K, Nemoto Y, Hiraide T, Suzuki K, Sadamatsu S, Adachi Y, et al. A strategy to predict the fracture toughness of steels with a banded ferrite–pearlite structure based on the micromechanics of brittle fracture initiation. Acta Mater 2018;144:386–99.
[22] Namegawa T, Hoshino M, Fujioka M, Minagawa M. Effect of Carbon Content on Toughness of Tempered Martensitic Steels Analyzed by Toughness Prediction Model. ISIJ Int 2019;59(7):1337–43.
[23] Kunigita M, Aihara S, Kawabata T, Kasuya T, Okazaki Y, Inomoto M. Prediction of Charpy impact toughness of steel weld heat-affected zones by combined micromechanics and stochastic fracture model – Part I: Model presentation. Engng Fract Mech 2020;230:106965.
[24] Mohseni P, Solberg JK, Karlsen M, Akselsen OM, Østby E. Investigation of mechanism of cleavage fracture initiation in intercritically coarse grained heat affected zone of HSLA steel. Mater Sci Technol 2012;28(11):1261–8.
[25] Keehan E. Effect of Microstructure on Mechanical Properties of High Strength Steel Weld Metals, PhD thesis, Göteborg, Sweden; 2004.
[26] Tomita Y. Improved fracture toughness of ultrahigh strength steel through control of non-metallic inclusions. J Mater Sci 1993;28(4):853–9.
[27] Guo F, Wang X, Liu W, Shang C, Misra RDK, Wang H, et al. The Influence of Centerline Segregation on the Mechanical Performance and Microstructure of X70 Pipeline Steel. Steel Res Int 2018;89(12):1800407.
[28] Echeverría A, Rodriguez-Ibabe JM. Brittle fracture micromechanisms in bainitic and martensitic microstructures in a C-Mn-B steel. Scr Mater 1999;41:131–6.
[29] Popovich VA, Richardson IM. Fracture toughness of welded thick section high strength steels and influencing factors. In: The Minerals, Metals & Materials Society, editor. TMS 2015 144th annual meeting & exhibition. pp. 1031–1038.
[30] Wallin K, Yamamoto M, Ehrnstén U. Location of initiation sites in fracture toughness testing specimen – the effect of size and side grooves. In: Proceedings ASME 2016 press vessel pip conference, ASME, Vancouver; 2016. p. 1–9.
[31] Pallaspuro S, Mehtonen S, Kömi J, Zhang Z, Porter D. Materials Science & Engineering A Effects of local grain size and inclusions on the low-temperature toughness of low-carbon as-quenched martensite. Mater Sci Engng, A 2019;743:611–22.
[32] Wallin K, Nevasmaa P, Laukkanen A, Planman T. Master Curve analysis of inhomogeneous ferritic steels. Engng Fract Mech 2004;71(16–17):2329–46.
[33] Andrieu A, Pineau A, Besson J, Ryckelynck D, Bouaziz O. Bimodal Beremin-type model for brittle fracture of inhomogeneous ferritic steels : Theory and applications. Engng Fract Mech 2012;95:84–101.
[34] Lin T, Evans AG, Ritchie RO. A Statistical Model of Brittle Fracture by Transgranular Cleavage. Mrch. Phys. Solids 1986;34(5):477–97.
[35] Martín-Meizoso A, Ocaña-Arizcorreta I, Gil-Sevillano J, Fuentes-Pérez M. Modelling cleavage fracture of bainitic steels. Acta Metall Mater 1994;42(6):2057–68.
[36] Lambert-Perlade A, Gourgues AF, Besson J, Sturel T, Pineau A. Mechanisms and modeling of cleavage fracture in simulated heat-affected zone microstructures of a high-strength low alloy steel. Metall Mater Trans A 2004;35(13):1039–53.
[37] Chen JH, Cao R. Micromechanism of cleavage fracture of metals. Elsevier; 2015.
[38] Jiang Q, Bertolo VM, Popovich VA, Sietsma J, Walters CL. Relating local stress on a hard microstructural inclusion from far-field stress on matrix to understand cleavage fracture in high strength steel. Int J Fract 2021;232:1–21.
[39] Griffith AA. The Phenomena of Rupture and Flow in Solids. Philos Trans Roy Soc A: Math Phys Engng Sci 1921;221:163–98.
[40] Bertolo VM, Jiang Q, Walters CL, Popovich VA. Effect of Microstructure on Cleavage Fracture of Thick-Section Quenched and Tempered S690 High-Strength Steel. In: Li J. et al., editors. Characterization of minerals, metals, and materials; 2020. p. 155–68.
[41] Bertolo VM, Jiang Q, Scholl S, Petrov R, Hangen U, Walters CL, et al. A Comprehensive Quantitative Characterisation of the Multiphase Microstructure of a Thick-Section High Strength Steel. J Mater Sci 2022.
[42] ISO 6892-3. Metallic materials – Tensile testing – Part 3: Method of test at low temperature; 2015.
[43] Dao M, Chollacoop N, Van Vliet KJ, Venkatesh TA, Suresh S. Computational modeling of the forward and reverse problems in instrumented sharp indentation. Acta Mater 2001;49(19):3899–918.
[44] ISO 12135. Metallic materials – Unifed method of test for the determination of quasistatic fracture toughness; 2018.
[45] Andrieu A, Pineau A, Besson J, Ryckelynck D, Bouaziz O. Beremin model: Methodology and application to the prediction of the Euro toughness data set. Engng Fract Mech 2012;95:102–17.
[46] Ray A, Sivaprasad S, Chakrabarti D. A Critical Grain Size Concept to Predict the Impact Transition Temperature of Ti-Microalloyed Steels. Int J Fract 2012;173(2):215–22.
[47] Ghosh A, Ray A, Chakrabarti D, Davis CL. Cleavage initiation in steel: Competition between large grains and large particles. Mater Sci Engng, A 2013;561:126–35.
[48] Gao X, Dodds RH. Constraint effects on the ductile-to-brittle transition temperature of ferritic steels: a Weibull stress model. Int J Fract 2000;102(1):43–69.
[49] Rosahl K, Booker JD, Lewis S, Smith DJ. A statistical approach for transferring fracture events across different sample shapes. Engng Fract Mech 2011;78(1):47–59.
[50] Ruggieri C. A modified local approach including plastic strain effects to predict cleavage fracture toughness from subsize precracked Charpy specimens. Theor Appl Fract Mech 2020;105:102421.
[51] Sherry AH, France CC, Gpldthorpe MR. Dimensional cracked geometries. Fatigue Fract Engng Mater Struct 1995;18(1):141–55.
[52] Hancock JW, Mackenzie AC. On the mechanisms of ductile failure in high-strength steels subjected to multi-axial stress-states. J Mech Phys Solids 1976;24(2–3):147–60.